Chap. 8 : Phonons and Relaxations in Unfilled Tetragonal Tungsten-Bronzes

Elena Buixaderas (1) and Jan Dec (2)

(1) Departments of Dielectrics, Institute of Physics, The Czech Academy of Sciences, 18221 Prague 8, Czech Republic,

(2) Institute of Materials Science, University of Silesia, Pl-40-007 Katowice, Poland

Corresponding author : buixader@fzu.cz

Abstract : The lead-free unfilled tetragonal tungsten-bronzes SBN and CBN are investigated by Raman, infrared and high-frequency dielectric spectroscopies. The substitution in the different channels affects phonons as well as relaxations. Relaxations in SBN show similar qualitative behaviour on increasing Sr content and relaxor behaviour, but for the extreme relaxor samples all characteristic frequencies are higher with stronger contribution to the permittivity in the GHz-THz range is stronger. The presence of a soft anharmonic central mode in the THz range together with the slowing down of a relaxation from GHz to MHz ranges reveals the coexistence of displacive and order-disorder scenarios for the ferroelectric phase transition in this family.

Keywords: PHONONS, DIELECTRIC RESPONSE, FERROELECTRIC OXIDES, RELAXOR MATERIALS, TETRAGONAL TUNGSTEN-BRONZES

Cite this paper: E. Buixaderas and J. Dec, OAJ materials and Devices, vol 5(1) – chap No8 in "Perovskites and other Framework Structure Crystalline Materials", p 281 (Coll. Acad. 2021) DOI:10.23647/ca.md20202108

I. Introduction

Oxides with complex networks of oxygen octahedra are very perspective in the quest for multiple functionalities. The most representative example is the perovskite family ABO3, which is the most investigated structure among materials used for electronics due to its relative simplicity and the possibility to find theoretical models to explain its properties [1].

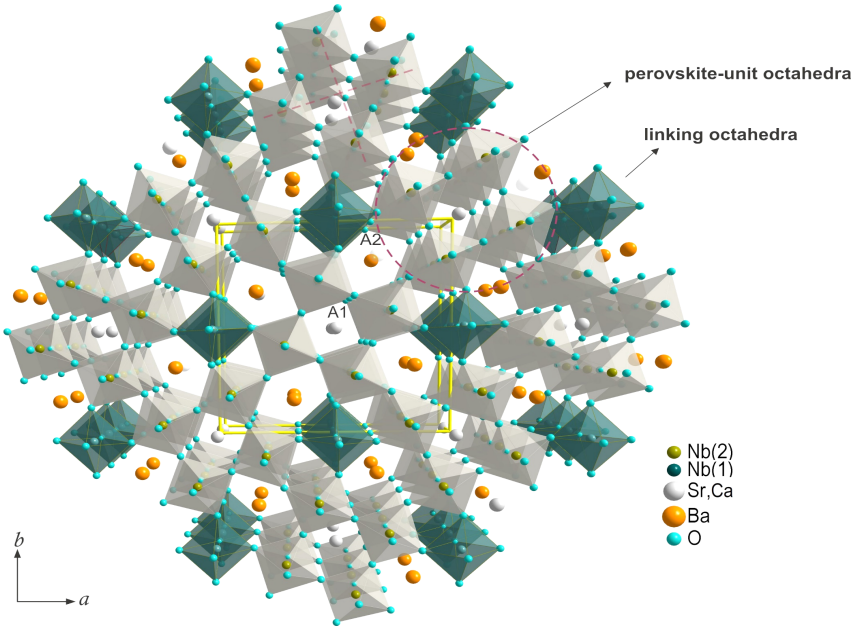

Figure 1: Tetragonal Tungsten Bronze structure of SBN and CBN

The structure of the unfilled TTB $(A1,A2)_6(B1_2B2_8)O_{30}$ in the paraelectric phase. The three types of channels are seen along the c-axis. Triangular ones are empty, and squared (A1 site) and pentagonal (A2 site) ones are filled with different cations. Two types of BO_6 octahedra (dark–linking and light-perovskite unit) correspond to the two different crystallographic sites (B1 and B2, respectively) available for the central atom and create two different sublattices. Yellow lines denote the unit cell. Red dashed circle marks the perovskite unit within the TTB structure.

There exist, however, other structures with interconnected octahedra that can also be very fruitful in providing alternatives for finding flexible properties and multiple responses with the advantage of having more atomic sites in their crystal lattice. For instance pyrochlore, layered perovskite, Aurivillius, and tungsten-bronze families [2-6]. This last family can have several variants, hexagonal, orthorhombic and tetragonal.

However, the tetragonal variation of the tungsten-bronze (abbreviated as TTB) is one of the most intensively studied system. The prototypic unit cell of TTB can be represented as $(A1,A2)_6C_4(B1_2B2_8)O_{30}$. This structure is formed by a network of corner-sharing oxygen octahedra, which form channels along its main axis (the *c*-axis) that can be filled with A1, A2 and C cations. Triangular channels are the smallest and can be filled just with small atoms like Li or K, but in many cases they are left empty. Only squared and pentagonal ones are filled, total or partially, by A1 and A2 atoms. Because of the flexibility of their dielectric properties, the family of *unfilled* TTBs has been studied more thoroughly, especially its major representative $(Sr_xBa_{1-x})_5Nb_{10}O_{30}$ SBN-X, with X=100x. SBN displays a perfect tuning between the conventional ferroelectric behaviour and the relaxor one, depending on the Sr amount present in the lattice [7]. Apart from many non-linear properties used in electro optics [8], SBN also exhibits one of the highest permittivity values among ferroelectric crystals [9]. Other possible applications of lead free TTB materials involve energy harvesting and storage devices [10,11] as well as voltage tuned capacitors [12].

Recently, important advances in the understanding of the ferroelectric and relaxor nature of the SBN family have been done, using high-frequency dielectric spectroscopy (10^4-10^{12} Hz), diffuse scattering and computer simulations[13, 14, 15]. The disordered nature of the family, caused by the random cationic substitution, vacancies in the channels and distortion of the oxygen octahedra network, leads to a complicated structure which favours incommensurate modulations and produces ultimately the relaxor behaviour in an indirect manner. The presence of two crystallographic sites for the Nb atom —Nb(1) at 2a sites, inside the so called linking octahedra grey colour in Fig. 1, and Nb(2) at 8h sites, inside the perovskite-like unit octahedra, dark green color in Fig. 1— has shown to be decisive in the development of the macroscopic polarization [15].

In these paper we report on various spectroscopic results (from Raman, IR, broad-band dielectric spectroscopies) obtained for two types of unfilled TTBs, SBN and $(Ca_xBa_{1-x})_6Nb_{10}O_{30}$ (CBN), aiming to compare the effects of the cationic substitution on the behaviour of phonons and relaxations, respectively.

II. Experimental methods

The SBN and CBN single crystals were grown by the Czochralski method. Details about the growth can be found elsewhere [7]. Platelets of a size about $4.5\times5\times0.8$ mm^3, with the polar axis oriented along one of the edges of the platelet, as well as prism and cylinders with the polar axis along the main axis, were cut from the bulk crystals to measure different types of phonons and relaxations using different experimental techniques:

II.1 Raman spectroscopy

Polarized Raman spectra were excited on the platelets with the 514.5 nm line of an Ar laser at a power of 25 mW (~ 4 mW on the sample) and recorded in back-scattering geometry using a RM-1000 Renishaw Raman microscope with a spectral resolution

better than 2 cm^{-1}. A grating filter enabled stray light rejection in the 10–900 cm^{-1} range and the diameter of the laser spot on the sample surface was about 2–3 μm. Temperature control of the samples from 80 to 800 K was carried with a Linkam THMS-600 cell. Spectra were corrected for the instrumental function of the microscope and the Bose-Einstein thermal factor [16].

II.2 Far-infrared (FIR) spectroscopy

Reflectivity measurements were performed on the same platelets using a Fourier spectrometer Bruker IFS 113v equipped with two room temperature DTGS pyroelectric detectors as well as He-cooled (1.5 K) Si bolometer. The light from a Hg lamp was polarized by a metal-mesh polarizer deposited on a thin polyethylene foil. For low temperature measurements (down to 12 K) a continuous-flow Oxford Optistat CF cryostat was used and the sample was mounted in a He gas bath, and for high temperatures (300–600 K) we used a custom-made oven. Room and high temperature spectra were measured in the range 30–1800 cm^{-1} with a resolution of 2 cm^{-1}. Due to the presence of polarizers and optical windows the accessible frequency range at low temperatures was 30–620 cm^{-1}.

II.3 Time domain transmission THz spectroscopy (TDTTS)

TDTTS measurements were carried out on thin polished plane-parallel samples ($4.5\times5\times0.05$ mm^3) with orientation (100) in the temperature range 10–800 K, using a polarized electromagnetic field to measure the E||c spectra. A custom-made time-domain THz transmission spectrometer was used to obtain the complex dielectric response from ~ 3 to 50 cm^{-1} with a resolution of 0.5 cm^{-1}. An Optistat CF cryostat with Mylar windows was used for measurements down to 10 K. An adapted commercial high-temperature cell Specac P/N 5850 without windows was used to heat the sample up to 800 K.

II.4 High-frequency dielectric spectroscopy

Dielectric measurements in the high-frequency range were taken on cylindrical samples of assorted dimensions cut from the bulk with the polar axis along the cylinder main axis. A computer controlled high-frequency dielectric spectrometer equipped with HP 4291B impedance analyser, a Novocontrol BDS 2100 coaxial sample cell and a Sigma System M18 chamber (temperature range 100–570 K) were used. Au electrodes were sputtered on the bases of the cylinders and the impedance of the samples was recorded at the cooling rate of 1 K/min.

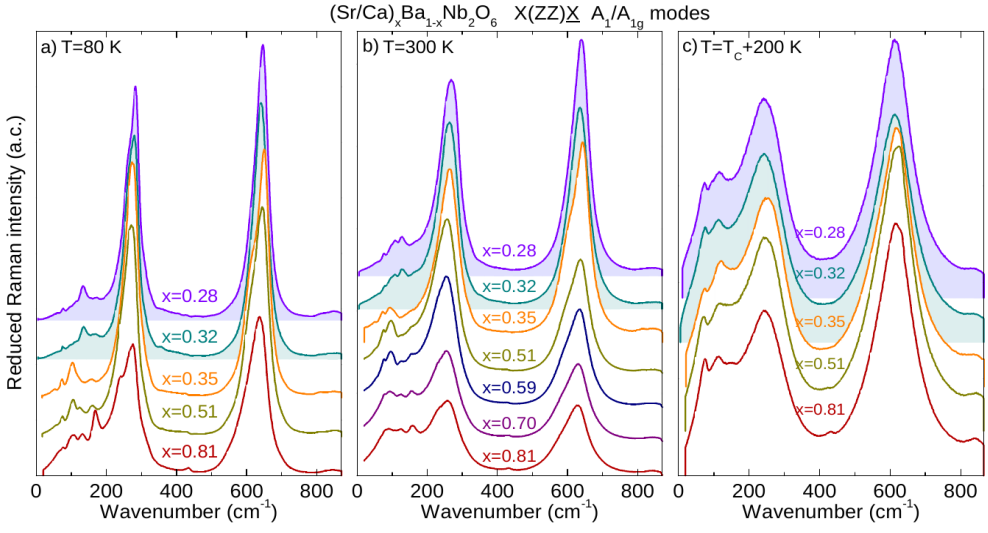

Figure 2: Raman spectra of SBN and CBN

Raman spectra of several SBN and CBN compositions reduced from the BE thermal factor in the X(ZZ)X geometry (Sr: x=0.81, 0.70, 0.61, 0.51, 0.35, Ca: x=0.32, 0.28), for selected temperatures 80 K (a), 300 K (b) and paraelectric phase (c). Shaded spectra correspond to CBN.

III. Results

III.1 Raman scattering of SBN and CBN

The Raman spectra for representative SBN and CBN compositions are shown in Fig. 2. All the displayed spectra correspond to the X(ZZ)X geometry –Porto's notation[17]– where A_1(TO) modes are active in the ferroelectric (Fig. 2a,b) and A_{1g}(TO) in the paraelectric phases (Fig. 2c), respectively. TO stands for transverse optic mode. The shaded spectra correspond to CBN. Spectra show three main parts. A low-frequency part with frequencies below about 200 cm^{-1}, where the external vibrations of cations outside the octahedra network are shown, and two main bands above, centred at 250 and 630 cm^{-1}. The last ones correspond to internal vibrations of the NbO_6 octahedra for almost all TTBs [18–24]: bending of O-Nb-O chains and stretching of Nb-O bonds.

One of the main problems to analyse phonons in these crystals is the great anharmonicity revealed in vibrations involving Nb and O. In addition, their frequency are close and modes are overlapped within the two strong bands. Because of this, the main differences in the Raman spectra arise from the external modes, well seen below

about 200 cm^{-1}. This can help to identify the individual cations in the structure. For instance, in SBN, modes from Sr have lower frequency ($\nu \sim 100 cm^{-1}$) than respective modes from Ca in CBN ($\nu \sim 130 cm^{-1}$). An exception concerns the vibration appearing at $\nu \sim 150\ cm^{-1}$, which might be due to the activated tilt of the oxygen octahedra, according to calculations in the related layered perovskite $Sr_2Nb_2O_7$ [25].

The temperature dependences of the Raman spectra on cooling for two selected compositions (SBN-81 and CBN-32) are depicted in Fig. 3. The changes in phonons are quite gradual and no sharp phase transitions are seen. In both cases new phonons appear in the ferroelectric phase, mainly at low temperatures and low frequencies, where the external modes due to vibrations of cations in the channels are seen (below 200 cm^{-1}). A proper site group analysis of the modes in SBN was published in [13].

Due to the relaxor nature of SBN-81 it is difficult to assess a finite temperature for the ferroelectric phase transition, although from [26] it is known that it should be around T ~ 310 K. The crystal CBN-32 is ferroelectric and has $T_C = 432$ K, nevertheless, the change in phonons is quite smooth too.

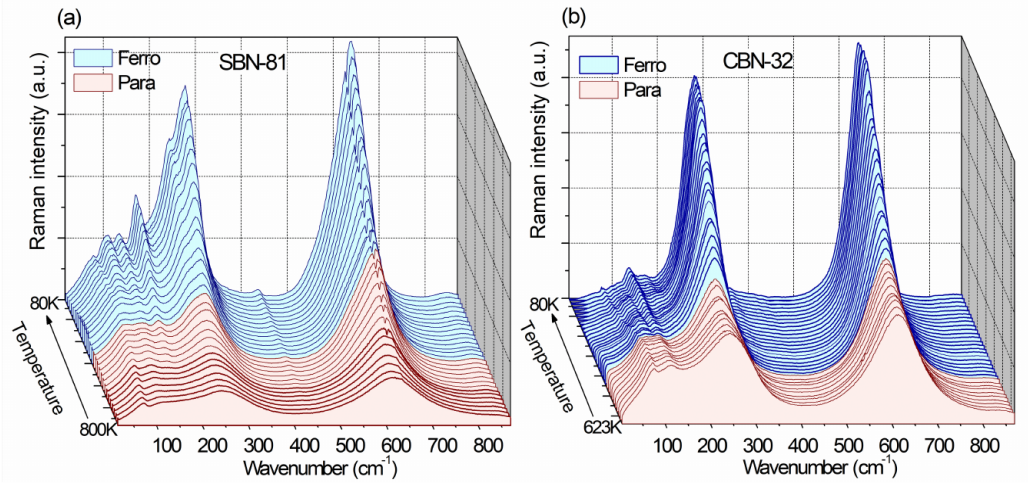

Figure 3: Temperature dependences of the Raman spectra of SBN-81 and CBN-32

Raman spectra of SBN-81 and CBN-32 collected on cooling in the X(ZZ)X, showing the A_{1g}/A_1 transverse modes. Spectra are corrected from the BE thermal factor.

The temperature dependences of the Raman frequencies for SBN-81 and CBN-32 are depicted in Fig. 4. The spectra look similar for both crystals but the relative intensity of the internal bands is weaker for SBN-81. Also this crystal shows a splitting of the band at ~250 cm^{-1} at lower temperatures. This probably indicates that the deformation of the NbO_6 octahedra is stronger for this relaxor composition. Consequently, it seems to be more affected by temperature than that CBN-32, where this effect is absent.

From the site group analysis, see Discussion and also [13], taking into account different sites for the Sr atoms, 11 A_{1g} modes are allowed in the paraelectric phase, from which 3 modes are due to external cations, and 8 are from internal modes of the NbO_6 octahedra.

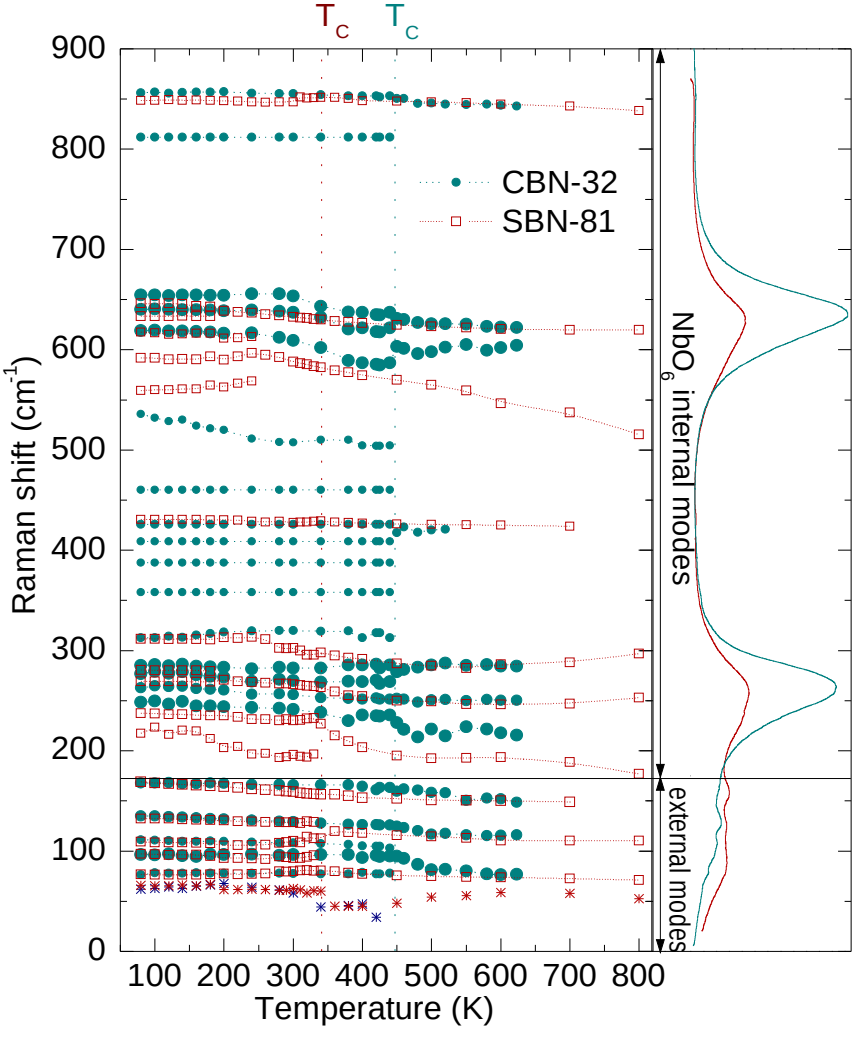

Figure 4: Temperature dependences of the Raman frequencies of CBN/SBN

The frequencies versus temperature of the Raman active A_g/A_1 modes of SBN-81 and CBN-32. And the spectra at room temperature in the right panel.

On the other hand, in the ferroelectric phase 21 A_1 modes are active (5 external and 16 internal). The site group analysis also allows identification of the sites involved, and therefore we know that in the paraelectric phase only the cations inside the pentagonal channels contribute to the Raman spectra (Sr and Ca in the squared channels are Raman inactive above T_C), and only Nb(2) in the perovskite-like units. For this reason, the two new modes that appear below T_C at low frequencies are due to Sr or Ca located at 2*a* sites in the squared channels.

In principle, CBN has no random occupation in the pentagonal channels, which are occupied solely by Ba [27], in contrast to SBN, where this site is shared by both Ba and Sr in the whole series. Due to this effect, the number of external active phonons should be lower [13]. Nevertheless the main phonons are similar for both materials, which might indicate that in our CBN crystals there is perhaps some Ca in the pentagonal channels too. Below 200 cm^{-1}, where the external vibrations from cations are detected in the paraelectric phase there are two modes. The lowest one correspond to Ba located in the pentagonal channels. As Ca in the squared channels should be not active in the para-phase, the mode at about 150 cm^{-1} could have different origin. It could be due to the presence of some Ca atoms in the pentagonal channels. Another possibility is that this mode is due to the tilt of the oxygen octahedra, similarly to the one appearing in the perovskite structure at similar frequencies [28].

The wide bands centred near 250 and 630 cm^{-1} correspond to internal modes of the NbO_6 octahedra (bending and stretching modes). Due to the high damping coefficients and the proximity of their frequencies it is difficult to resolve all the vibrations. This is especially true for SBN-81, where anharmonicity is higher, because of its relaxor character. At low temperatures, a close inspection of the spectra in CBN-32 allows to resolve several very week modes between 350 and 450 cm^{-1}.

All the investigated TTB crystals do not display a typical soft mode, although there is a central mode (CM) component that is present in all compositions below the lowest phonon and displays a temperature dependent behaviour. This excitation will be addressed later in more detail.

It is also interesting to compare the composition dependence of the cationic external modes for the whole SBN series. Fig. 5a illustrates the fits of the Raman spectra below 350 cm^{-1} at RT for various compositions, including the decomposition of the fit into individual oscillators. In Fig. 5b the individual frequencies of the modes used in the fit. Three blocks are found. The lowest modes are the CM and the Ba vibrations, the three middle ones are due to Sr –although the mode at 150 cm^{-1} could be also due to oxygen octahedra tilts–, and the upper block correspond to internal vibrations of NbO_6 octahedra inside the first strong band centred at 250 cm^{-1}. External modes frequencies are quite constant. Just the mode near 150 cm^{-1} shows higher frequency when increasing Sr content. The same happens with the internal modes. This could be due

to the smaller size of the unit cell for high Sr concentrations.

Fig 5c depicts the Raman strength of the modes, that is, the area below each peak. This quantity gives an idea of the strength of the oscillators and is useful to follow the influence of the Sr substitution. As Sr content increases, the strength of the modes related to Sr atoms should increase and the strength from Ba-related modes should decrease, which is clearly seen in the figure. For the internal modes, it is better to compare the overall strength of the band, which is depicted by the big black crossed diamonds.

This band is stronger in SBN-35 and losses strength for the higher contents of Sr, where Raman spectra are less intense.

III.2 FIR reflectivity of SBN and CBN

Another technique very useful to analyse the behaviour of the phonons is infrared spectroscopy, where complementary information to Raman spectroscopy is found. This particularly concerns the paraelectric phase of SBN and CBN.

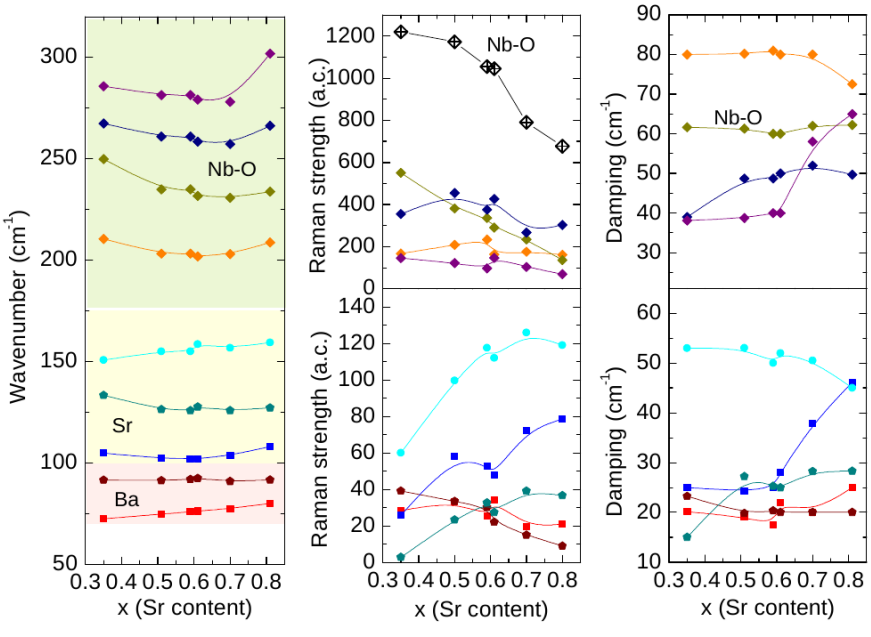

Figure 5: Composition dependences of the Raman parameters of SBN

Frequencies, Raman strength and damping of the Raman modes versus Sr content in SBN together with the decomposed fit of the spectra to show individual modes up to 350 cm^{-1}.

Polar phonons were detected in a reflection mode with a polarizer and samples oriented with the polar c axis along the crystals. Therefore solely A_1(TO) modes are detected in the ferroelectric phase. The FIR spectra at room temperature spectra and at about 60 K are shown in Fig. 6.

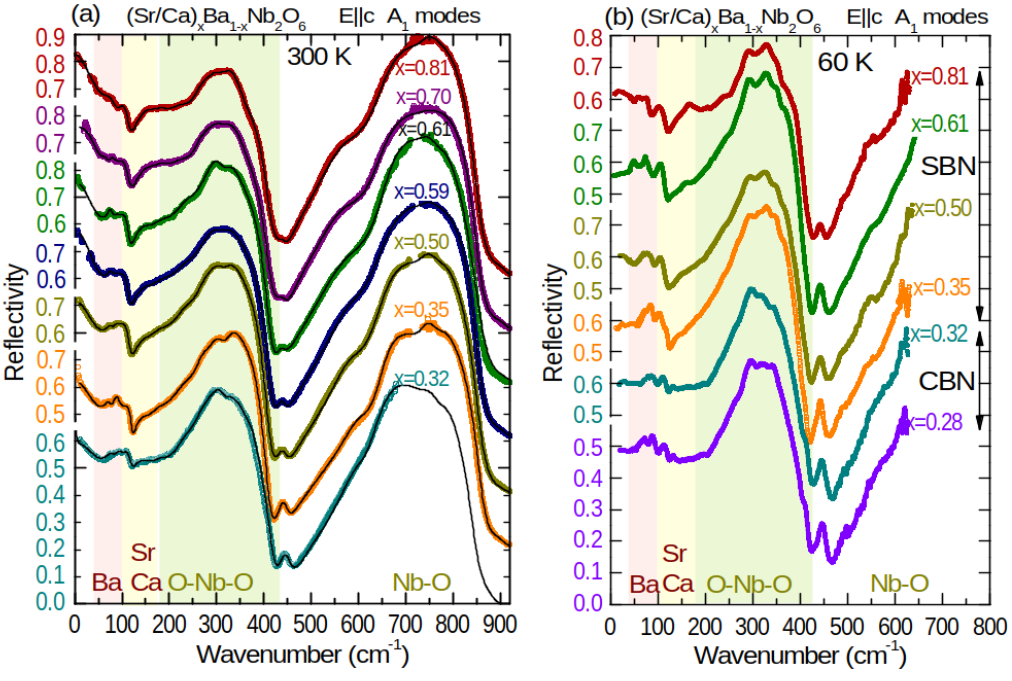

Figure 6: FIR reflectivity spectra of SBN and CBN

FIR reflectivity spectra of several SBN and CBN compositions with E||c (Sr: x=0.81, 0.70, 0.61, 0.51, 0.35, Ca: x= 0.32, 0.28), for selected temperatures (a) 30 K and (b) 60 K.

The spectra show three well defined regions, in accordance with the Raman experiment. Below ~200 cm^{-1} external vibrations from cations are detected. The internal octahedra vibrations correspond to the two broad reflectivity bands. Spectra were fitted with a generalized oscillator model [29].

$$\hat{\varepsilon}(\nu)=\varepsilon'(\nu)+i\varepsilon''(\nu)=\varepsilon_{\infty}\prod_{i=1}^{n}\frac{\nu_{LOi}^{2}-\nu^{2}+i\nu\gamma_{LOi}}{\nu_{TOi}^{2}-\nu^{2}+i\nu\gamma_{TOi}}\quad , \qquad (1a)$$

$$\Delta\varepsilon_i = \frac{\varepsilon_\infty}{\nu_{TOi}^2} \frac{\prod_j \left(\nu_{LOj}^2 - \nu_{TOi}^2\right)}{\prod_{j\neq i} \left(\nu_{TOj}^2 - \nu_{TOi}^2\right)} \quad , \qquad (1b)$$

where ε_∞ is the permittivity at frequencies much higher than all polar phonon frequencies, ν_{TOi} and ν_{LOi} are the transverse and longitudinal frequencies of the *i*-th phonon mode, γ_{TOi} and γ_{LOi} their respective damping coefficients; and $\Delta\varepsilon_i$ its contribution to the permittivity.

At low temperatures due to the lowering of the damping, phonons are better discerned, and even the internal modes of the NbO_6 octahedra are identified, in contrast to the Raman spectra where these vibrations were still hidden within the broad Raman bands (Fig. 1). All FIR spectra display an increase of reflectivity in the low frequency part, especially visible at 300 K. The data at these low frequencies were collected by the TDTTS experiment, and an extra excitation was added in order to fit the experimental points, the CM.

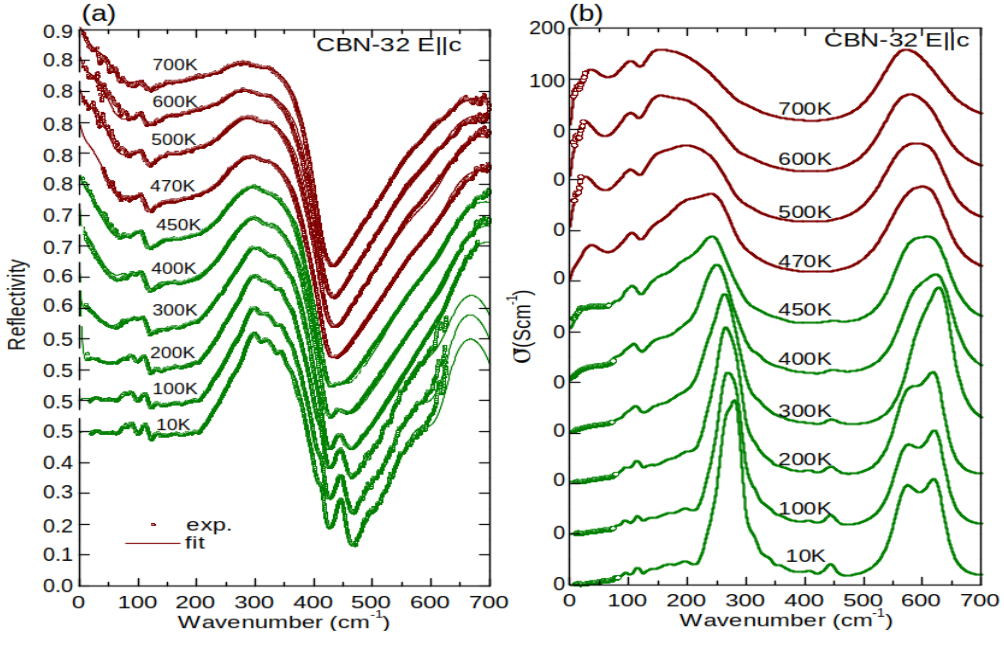

Figure 7: Temperature dependences of reflectivity and optical conductivity spectra of CBN-32

(a) Reflectivity of CBN-32 on cooling, scattered points correspond to the experiments including TDTTS experiment, lines correspond to the fits with eq. (1). (b) Optical conductivity $\sigma'(\nu)=2\pi c\varepsilon_0\nu\varepsilon''(\nu)$ calculated from the fits of the reflectivity and the TDTTS data using eq. (1) together with the experimental points.

This excitation below phonons is very anharmonic, mostly overdamped ($\gamma_{TO} \gg \nu_{TO}$) except at low temperatures. At low temperatures (Fig. 6a), the shape of the spectra differs significantly among the various compositions. It is even possible to recognize that the internal vibrations of the NbO_6 octahedra are slightly different for SBN and CBN. This means that the cationic environment in the channels affects the deformation of the oxygen octahedral cages. The temperature dependences of the reflectivity spectra of SBN-35, SBN-61 and SBN-81 had already been published together with TDTTS data[13,14,30]. The CBN family displays a very similar temperature dependence. Thus we chose to display here CBN-32 for illustration (Fig. 7).The reflectivity taken with E||c is depicted in Fig. 7a for several temperatures including the fits performed with eq. (1). The calculated optical conductivity $\sigma'(\nu) = 2\pi c \varepsilon_0 \nu \varepsilon''(\nu)$ is also shown (Fig. 7b), and it is worth noting that it resembles very much the shape of the Raman spectra of Fig. 3b.

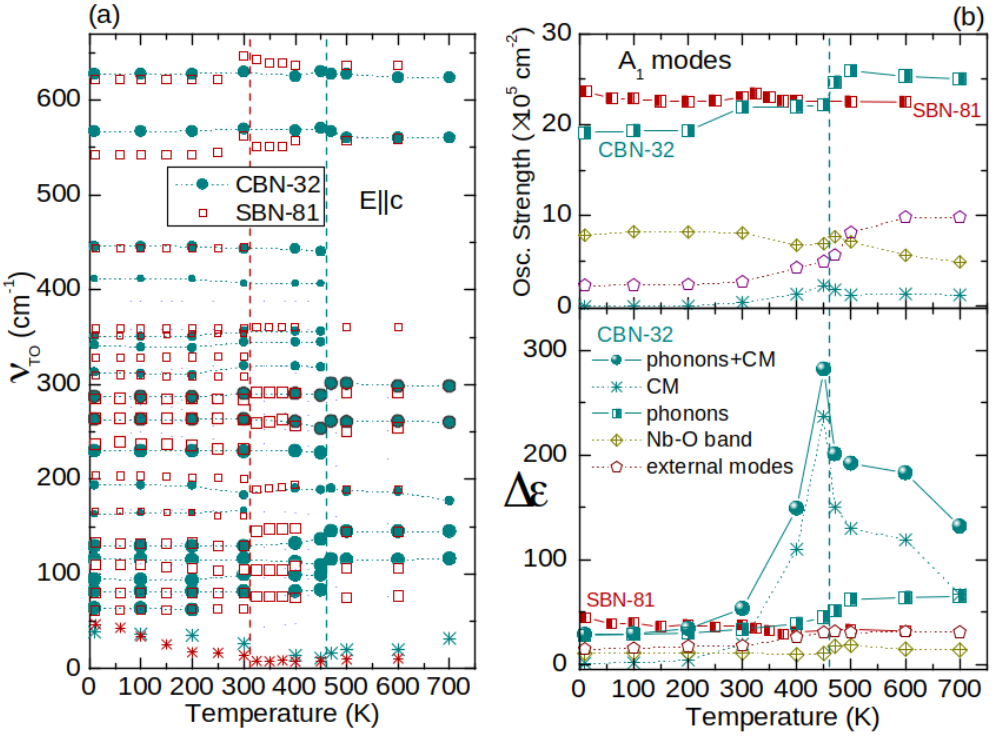

Figure 8: Temperature dependences of the IR phonon parameters in CBN/SBN

(a) Transverse optic frequencies of the main A_1 modes, (b) Contribution to the permittivity ($\Delta\varepsilon$) of the external and internal modes together with the overall phonon contribution, and oscillator strength of the same modes, including the total contribution of the Nb-O band.

Like in the case of SBN family, there is no optical soft mode, and the transition is driven by excitations of lower frequency. This can be seen in the temperature dependences of the IR modes (Fig. 8), and it is very similar to the one found in SBN. In the figure the frequencies of the modes of SBN-81 are also depicted. The intensity of the modes is proportional to the size of the symbols.

Both materials show splitting of phonons at their respective phase transitions, (T_C = 470 K for CBN-32 and T_C = 330 K for SBN-81), and the only excitation which displays softening towards T_C is the CM, marked by asterisks in Fig. 8a. This soft CM has been discussed in the SBN family [13] and it is related to the anharmonic motion of cations in the channels and within the oxygen octahedra.

Fig. 8b and c show the contribution to the permittivity $\Delta\varepsilon$ and the oscillator strength of some bands, calculated as $\nu^2\Delta\varepsilon$, for CBN-32, compared to SBN-81. In general, in both families of SBN and CBN, the contribution of phonons to the permittivity is quite small, about 40–50, and it does not show any significant anomaly at T_C. On the contrary the excitation just below phonons, the CM at THz frequencies displays already an anomaly in frequencies and also in permittivity that explains, at least partially, the behaviour in the vicinity of the phase transition point. This behaviour is very similar to that found in SBN, where the CM plays an important role in the phase transition and its contribution to the permittivity changes with the Sr content, being much stronger for relaxor composition with contents higher that 60% [14].

The above analysis of the experimental data allows us to say that the total oscillator strengths of phonons in SBN and CBN are similar for both families and do not display any marked anomaly, apart from a decrease around T_C in CBN-32. The contribution from the external and the internal modes can be displayed separately, as well as their oscillator strengths. External cations have a higher contribution to permittivity than internal modes of the NbO_6 octahedra, but this is reversed in their oscillator strength values below T_C.

The compositional dependence of the IR phonons in the SBN family (Fig. 9) shows a trend similar to the one displayed by the Raman phonons. This is due to the fact that the same phonons are simultaneously Raman and IR active. IR frequencies are practically constant for all the SBN compositions (Fig. 9a). Modes related to Sr vibrations have stronger oscillator strength and contribution to permittivity for high Sr compositions. However, there is a difference in the behaviour of the bending Nb-O band. The IR band keeps its contribution to the permittivity and its oscillator strength constant across the compositional diagram (Fig. 9b,c), whilst the equivalent Raman band loses its Raman strength for higher contents of Sr due to a lower scattering signal.

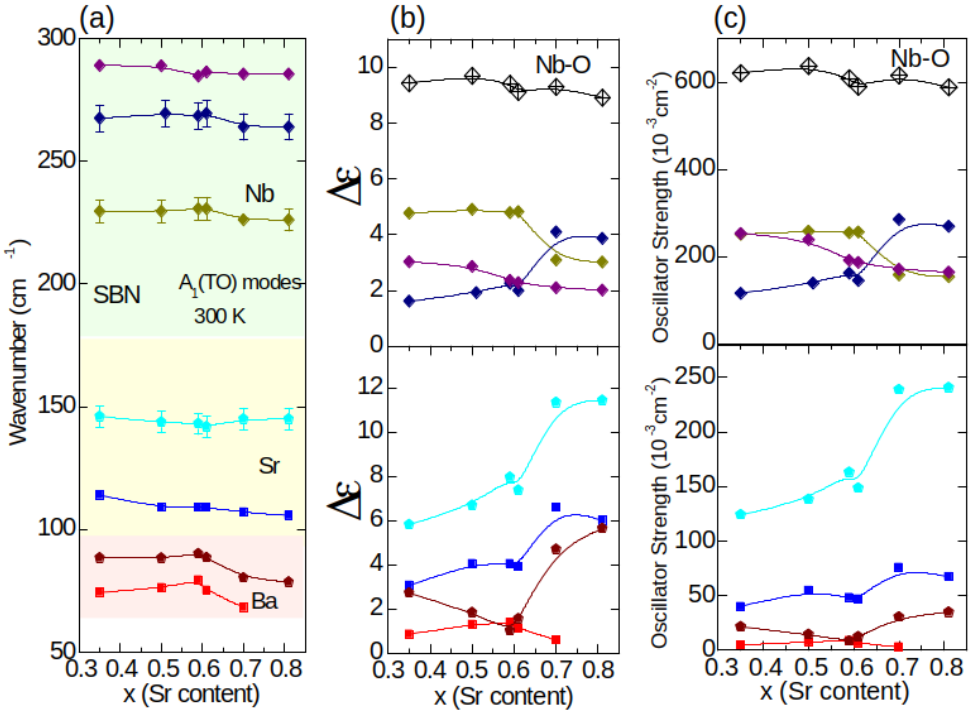

Figure 9: Compositional dependences of the IR phonon parameters in SBN

(a) Transverse optic frequencies of the main A_1 modes, (b) Dielectric strength–contribution to the permittivity of the individual modes together with the overall contribution for the Nb-O band, and (c) Oscillator strength of the same modes, including the total contribution of the Nb-O band.

III.3 High-frequency dielectric response of SBN

As found in our previous papers[13,14,30,31], the ferroelectric phase transition in SBN, and in general in TTBs, is mainly driven by excitations of frequencies lower than those of phonons. Besides the CM at THz frequencies there are at least two strong relaxations between kHz and GHz that carry the main contributions to the permittivity and, thus, to the dielectric anomaly.

In Figs. 10 and 11 the dielectric response between 10 kHz and THz is displayed for the ferroelectric SBN-35 crystal [13] and relaxor SBN-81 one [14]. The dependences of ε' and ε'' with temperature (Fig. 10) show the ferroelectric and relaxor behaviour as the two extremes in the SBN family. CBN crystals were not measured below the kHz range, but at lower frequencies they do not display strong relaxor behaviour [32].

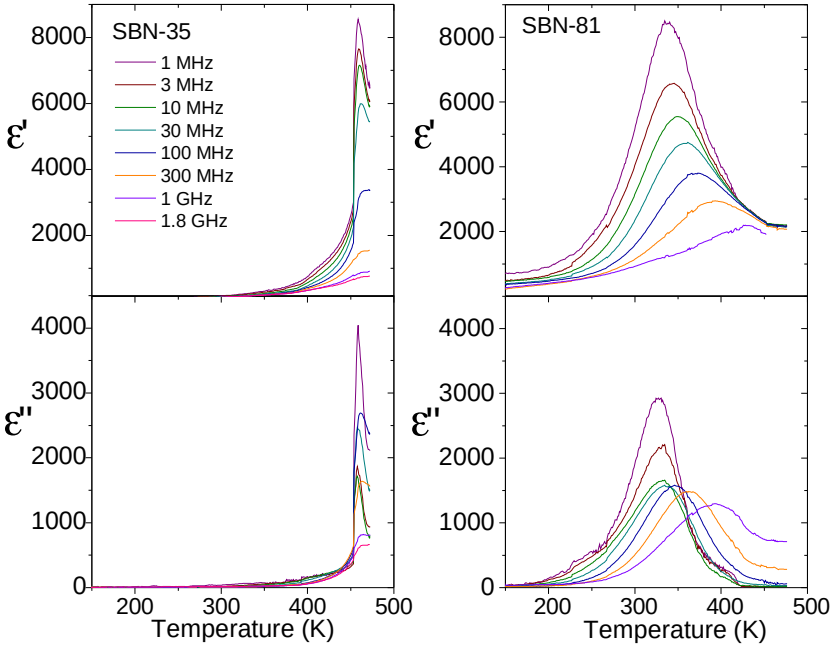

Figure 10: Temperature dependences of the complex permittivity in SBN

(a) Temperature dependences of the permittivity and dielectric loss between MHz and GHz in (a) ferroelectric SBN-35, where a sharp transition is seen, and in (b) relaxor SBN-81, where the temperature dependence of the maxima are clearly depicted.

When analysing the frequency dependences of the complex permittivity $\varepsilon(\nu)=\varepsilon'(\nu)-\varepsilon''(\nu)$ (Fig. 11) the excitations at frequencies below those of phonons become noticeable. They were analysed with a model that combines Cole-Cole relaxations and damped harmonic oscillators [31]:

$$\hat{\varepsilon}(\nu)=\sum_j \frac{\Delta\varepsilon_{0j}}{1+(i\nu/\nu_{0j})^{1-\alpha_j}}+\sum_k \frac{\Delta\varepsilon_k \nu_k^2}{\nu_k^2-\nu^2+i\gamma_k\nu}+\varepsilon_\infty \qquad (2)$$

$\Delta\varepsilon_{0j}$ denotes the dielectric strength of the *j*-th relaxation, ν_{0j} its characteristic frequency, α_j is a real exponent between 0 and 1, which describes the increase of width of the loss peak in the frequency dependences and determines the deviation from the pure Debye model. In the oscillator term, ν_k and γ_k refer to the frequency and damping constant of the *k*-th oscillator, and ε_∞ stands for the electronic contribution at frequencies above the phonon range. For the considered TTBs ε_∞ is of the order of 10

and the overall phonon contribution ranges between 30–50, depending on the temperature.

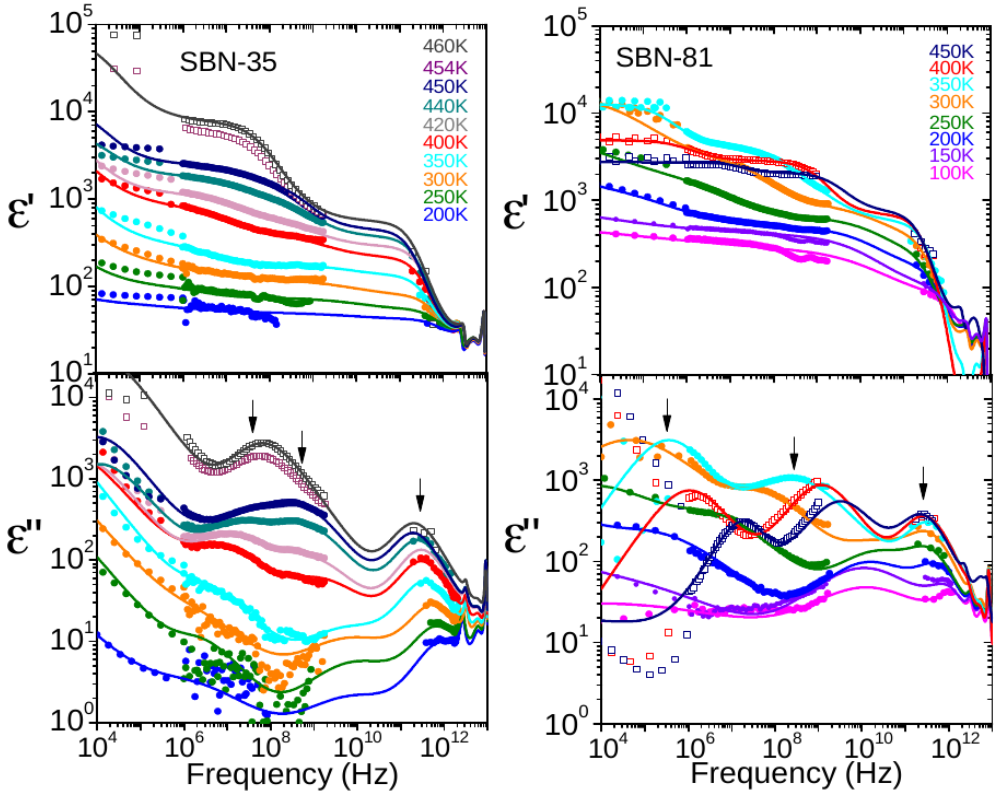

Figure 11: Frequency dependences of the complex permittivity in SBN

Frequency dependences of the permittivity and dielectric loss for various temperatures in (a) ferroelectric SBN-35, and in (b) relaxor SBN-81. Arrows denote the maxima of the dielectric loss corresponding to different excitations.

In all the studied composition three main excitations appear at frequencies below those of phonons, labelled as:

(a) ν_{THz}, a central mode type excitation, corresponding to a very anharmonic motion, located at THz frequencies

(b) ν_{GHz}, an excitation that appears below or near T_C in different compositions in the GHz range, showing a weak temperature dependence on cooling, and it can be modelled with relaxation or a damped oscillator depending on the crystals.

(c) ν_{01}, a relaxation that slows down from GHz to kHz on cooling and exhibits the

strongest contribution to the permittivity.

At lower frequencies more relaxations are present. For instance in SBN-81 there are at least two, located at kHz and mHz ranges, related to the breathing of needle-like polar nanoregions perpendicular and parallel to the polar axis [33]. The existence of nanoscale objects, in the form of polar fluctuations of nanoscale size, has been confirmed in x-ray and neutron diffuse scattering [34-37]. Even more, no spatial correlations were found between the chemical ordering and the existing polar nanoregions in canonical relaxors like PMN [37]. Similar behaviour is expected to take place in the investigated TTB materials.

The qualitative behaviour of the SBN family is similar for all the compositions. As found in [13,14,31] several polarization mechanisms with different characteristic frequencies contribute to the overall dielectric response. The main differences arise in the frequencies of the involved excitations and their individual contribution to the permittivity. It was found that for SBN-81, the utmost relaxor composition with the smallest polar nanodomains, the frequencies of all non phononic excitations are higher.

IV. Discussion

CBN is not a relaxor ferroelectric, although the ferroelectric phase transition shows some signs of diffusivity, like a slightly broadened permittivity maximum [32]. Crystallographic data in some crystals [27] found that it has not random occupancy in the pentagonal channels: all Ca atoms go to the squared channels and Ba only is present in the pentagonal ones. Compared to the SBN solid solution, CBN should be similar to SBN-35. Yet, CBN has much smaller domains [38,39] and shows higher level of disorder than SBN-35. The relaxor behaviour in SBN for higher Sr compositions is partially caused by the random occupation of the pentagonal channels, and the size of the ferroelectric domain decreases with increasing Sr content, along with the relaxor behaviour [40].

IV.1 Comparison of IR-Raman phonons

The comparison of the Raman and IR phonons, which are complementary active in the paraelectric phase and simultaneously active in the ferroelectric phase can give a hint about the occupation of the channels.

The site group analysis of ref [13] revealed that the double occupancy of the pentagonal channels leads to the appearance of extra external modes at low frequencies, corresponding to vibrations of the cations in the unit cell, due to the different mass of Sr and Ba. This kind of consideration has not been taken into account in the literature previously.

Table 1 : Site group analysis for external modes in CBN/SBN

Para-phase *P*4/*mbm*		
Atom	Site	Modes
Ca/Sr1	2a □	A_{1u}(-) + **A_{2u}(c)** + 2E_u(a,b)
-/Sr2	4g ⬠	**A_{1g}(*aa bb cc*)** + **A_{2u}(c)**+ E_u(a b) + E_g(*ac bc*) + B_{1g}(*aa bb*) + B_{2g}(*ab*) + A_{2g}(-)+B_{1u}(-)
Ba	4g ⬠	**A_{1g}(*aa bb cc*)**+**A_{2u}(c)**+ 2E_u(a b)+E_g(*ac bc*)+B_{1g}(*aa bb*) +B_{2g}(*ab*)+A_{2g}(-)+B_{1u}(-)
Ferro-phase *P*4*bm*		
Atom	Site	Modes
Ca/Sr1	2a □	**A_1(c, *aa bb cc*)** + 2E(a b, *ac bc*) + A_2(-)
-/Sr2	4c ⬠	**2A_1(c, *aa bb cc*)** + 3E(a b, *ac bc*) + B_1(-, *aa bb*) + 2B_2(-,*ab*)+ A_2(-)
Ba	4c ⬠	**2A_1(c, *aa bb cc*)** + 3E(a b, *ac bc*) + B_1(-, *aa bb*) + 2B_2(-, *ab*)+ A_2(-)

However for the correct interpretation of the Raman and IR spectra it is required: it sheds light about how the whole lattice vibrations behaves and about the occupation of the channels, which is a very important element in the interpretation of the dielectric response of TTBs. For clarity we show these modes in Table 1. Bold type refers to the modes active along the polar axis. IR and Raman activities are in parenthesis: single letters a, b and c refer to IR activity, double letters, *aa* or *ab*, *ac* etc refer to Raman activity.

For the simple occupation case (as presumed in CBN), the external modes at the centre of the unit cell (Γ point) are:

$\Gamma_{ext\ para}$[CBN] = Γ[Ca(2*a*)+Ba(4*g*)] =

A_{1g}(*aa bb cc*) + **2 A_{2u}(c)** + 4E_u(a,b) + E_g(*ac bc*) + B_{1g}(*aa bb*) + B_{2g}(*ab*) + A_{1u}(-) + A_{2g}(-) + B_{1u}(-)

$\Gamma_{ext\ ferro}$[CBN] = Γ[Ca(2*a*)+Ba(4*c*)] =

3 A_1(c, *aa bb cc*) + 5E_u(ab, *ac bc*)+ B_1(-, *aa bb*) + 2B_2(-, *ab*) + 2A_2(-)

and for the double occupation case (as in SBN):

$\Gamma_{ext\ para}$[SBN] = Γ[Sr1(2*a*)+Sr2(4*g*)+Ba(4*g*)] =

$2A_{1g}$(*aa bb cc*) + **$3A_{2u}$(c)** + $6E_u$(a,b) + $2E_g$(*ac bc*) + $2B_{1g}$(*aa bb*) + $2B_{2g}$(*ab*) + A_{1u}(-) + $2A_{2g}$(-) + $2B_{1u}$(-)

$\Gamma_{ext\ ferro}$[SBN] = Γ[Sr1(2*a*)+Sr2(4*c*)+Ba(4*c*)] =

$5A_1$(c, *aa bb cc*)+ $8E_u$(ab, *ac bc*)+ $2B_1$(-, *aa bb*) +$4B_2$(-, *ab*)+ $3A_2$(-)

In Figs. 2 to 8 all the spectra were recorded with the polarization of the crystal parallel to the incoming electromagnetic field. In this case the modes selected were just A_{1g}/A_1 in the Raman spectra and A_{2u}/A_1 in the IR spectra. This means that, theoretically, in CBN we expect in the Raman spectra of the paraelectric phase $1A_{1g}$ mode related to Ba in the pentagonal channels and no modes related to Ca in paraelectric phase. While in the ferroelectric phase 3 A_1 modes from Ca and Ba are active. The new two modes should stem from the two modes IR active in the paraelectric phase. A closer look at Figs. 2 and 4, reveals that in the paraelectric phase of CBN there is more than one A_{1g} mode, which probably means that there is also mixed occupation in the pentagonal channels, although small enough not to be detected by x-ray experiments.

For SBN, the Raman spectra should show in paraelectric phase $2A_{1g}$ modes (corresponding to both Ba and Sr in the pentagonal channels) and in the ferroelectric phase 5 A_1 modes. The group analysis also shows that the 3 extra modes appearing should stem from the three A_{2u} IR active modes in the paraelectric phase.

In SBN the comparison of the frequencies and the strength of cationic modes on the Sr content can serve to assign the modes. An inspection of the parameters presented in Table 2 reveals that at high temperatures in the paraelectric phase, where the modes are either IR or Raman active, the IR active mode at ~100 cm^{-1} should be due to Sr in squared channels. As there is more Sr in SBN-81 its strength should be higher for this composition, which is indeed the case. Therefore the other IR mode at 150cm^{-1} should be due to Sr in pentagonal channels and it should be also Raman active, which is the case.

Table 2 shows the frequencies of all detected modes below 200 cm^{-1} in IR and Raman spectra for SBN-35, SBN-81 and CBN-32 in the paraelectric phase (500 K) and in the ferroelectric phase (100 K). The principal facts that can be established from the table are:

- the paraelectric phase in SBN-81 and CBN-32 show more Raman active external modes than predicted by theory. This can be attributed to the higher disorder in these crystals.

Table 2 : Frequencies of the external modes in CBN/SBN

T(K)	Composition	IR (cm^{-1}) A_{2u}/A_1	Raman (cm^{-1}) A_{1g}/A_1	Atom
500	SBN-35	77.0	68.62	Ba
		109.5	--	Sr1
		152.1	126.3	Sr2
	SBN-81	75.0	75.3	Ba
		106.0	111.5	Sr1
		144.0	150.2	Sr2
	CBN-32	--	84.6	Ba
		115.0	116.2	Ca
		145.2	153.4	Ca2
100	SBN-35	75.3	72.9	Ba
		90.2	98.5	Ba
		110.7	105.8	Sr1
		116.0	120.0	Sr2
		161.7	156.8	Sr2
	SBN-81	62.3	68.4	Ba
		80.3	76.4	Ba
		109.7	107.6	Sr1
		131.9	132.3	Sr2
		165.7	168.1	Sr2
	CBN-32	64.0	60.4	Ba
		81.8	77.7	Ba
		94.0	106.7	Ca1
		129.4	135.3	Ca2
		164.5	167.6	Ca2

- CBN-32 has the same active modes as SBN, which confirms that it should be some Ca occupancy also in the pentagonal channels.

- in the ferroelectric phase the modes are simultaneously IR and Raman active and

have practically coincident frequencies, which supports the validity of the site group analysis.

The internal modes of the NbO_6 octahedron appear above ~200 cm^{-1}. These modes are present in numerous structures formed by oxygen octahedra networks. The O–Nb–O bending and Nb–O stretching vibrations were already tabulated by Nakamoto [41] and analysed by Ross in the case of barium sodium niobate (BNN) [42], and from the analysis we can assign the bands found in our experimental spectra. These vibrations are depicted in Fig. 12 and their assignments and frequencies are listed in Table 3.

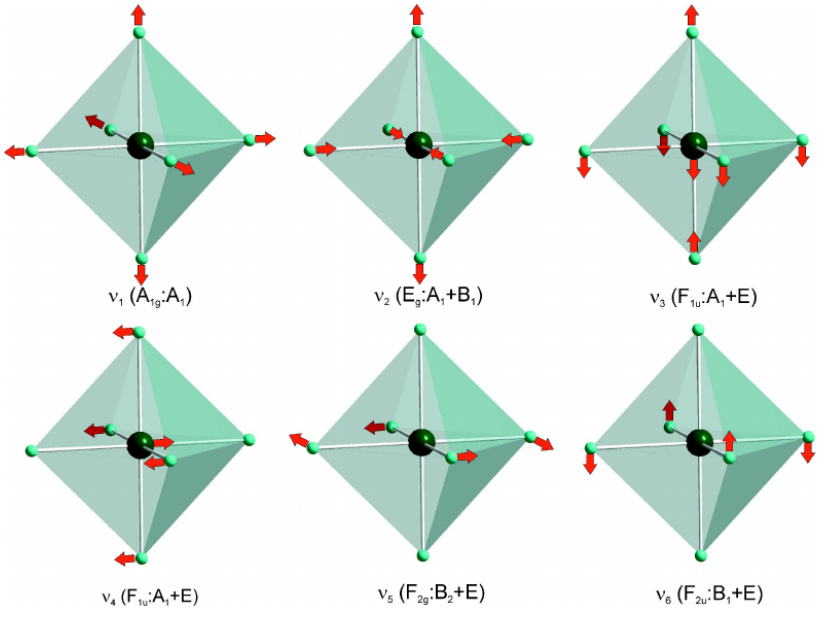

Figure 12: Internal modes of the NbO_6 octahedra

From Table 3 it is possible to see that, in the tetragonal environment, most of the internal modes are split and they are in general both Raman and IR active. For the symmetries studied in our samples, where just modes with polarization parallel to the polar axis were detected, the majority of the internal modes A_1 modes should be located at frequencies above 300 cm^{-1}.

As these modes were better discerned by the IR experiment at very low temperatures, we display in Table 4 a list of the frequencies found between 200 and 700 cm^{-1}, with a comparison with the frequencies fitted in the Raman experiment.

Table 3 : Assignment of the internal NbO_6 modes in TTBs[42]

		Symmetry Cubic:Tetragonal	Frequency (cm^{-1})
Breathing	ν_6	F_{2u}(-): B_1(R)+E(IR,R)	160
Bendings	ν_5	F_{2g}(R):B_2(R)+E(IR,R)	290
	ν_4	F_{1u}(IR):A_1(IR,R)+E(IR,R)	320
Stretchings	ν_3	F_{1u}(IR):A_1(IR,R)+E(IR,R)	650
	ν_2	E_g(R): A_1(IR,R)+B_1(R)	550
	ν_1	A_{1g}(R):A_1(IR,R)	660

Modes above 700 cm^{-1} are not listed, as the window of the cryostat in the IR experiments set up does not allow to measure beyond that. Also the frequencies found in the related compound $Sr_2Nb_2O_7$ (SNO) by IR reflectivity [43] are shown. In bold we highlight the more intense bands.

In total 16 internal A_1 modes are allowed in the ferroelectric phase [14,18]. Most of them were detected by the IR experiment. Bending modes split from the ν_4 mode are detected within the wide IR and Raman band located between 200 and 450 cm^{-1}. There are 4 modes, more intense whose frequencies coincide very well between both experiments. The stretching modes stemmed from ν_1, ν_2 and ν_3 are more difficult to identify due to the experimental restrictions in the IR measurements and the high damping of the vibrations in the Raman spectra (even at the lowest temperatures). Despite of this, at least three modes are detected in all the measured TTBs with both techniques, being the more intense the mode at ~ 650 cm^{-1}.

As these internal modes should be common to all oxides whose structure is built from NbO_6 octahedra. We can compare also these frequencies with the measured in the related compound SNO [43]. At room temperature, in the tetragonal phase, 17 A_1 modes above 150 cm^{-1} were measured by IR reflectivity. These phonons are much sharper than in SBN or CBN.

These frequencies also agree quite well with the ones calculated by density functional theory for the same compound [25], which points out that the NbO_6 octahedra network in TTBs indeed operates as an independent entity and metallic cations embed in the channels vibrate against it without interacting among them. This specific behaviour affects the dielectric response and the rest of the excitation present in the material at lower frequencies.

Table 4 : Frequencies of the internal A_1 modes in SBN/CBN at low temperatures, compared to those of $Sr_2Nb_2O_7$ in the tetragonal phase

	Frequency IR (10 K)				Frequency Raman (80 K)		
	SNO (300 K)	SBN-35	SBN-81	CBN-32	SBN-35	SBN-81	CBN-32
ν_4	178.1	188.2	204.6	194.0	206.4	190.0	
						217.6	
	228.0	**235.8**	**237.0**	**229.8**	**234.5**	**237.4**	**248.5**
					252.9		262.8
	240.3	**264.4**	**264.5**	**263.1**	**268.1**	**269.3**	**276.7**
	272.7	**287.9**	**284.5**	**287.3**	**281.7**	**280.6**	**285.3**
	298.0						
	315.4	**311.0**	**309.2**	**313.0**	**305.8**	**311.7**	**312.7**
	338.2	320.1	327.7	341.5			
	358.5	345.5	351.9	351.0			
	387.3	357.0	358.5				358.2
	418.2	404.8		411.6			408.7
	452.8	440.7	444.0	445.6	425.0	430.5	425.8
ν_3	527.3						535.9
ν_2	569.4	553.0	542.1	567.4		559.2	
ν_1	597.0	601.1				591.7	
			622.1	627.5	614.2	617.4	619.1
					640.6	633.5	640.3
	683.4	**653.5**			**653.6**	**646.1**	**654.4**
					808.7		811.9
	842.1					848.5	
	860.6				853.9		856.2

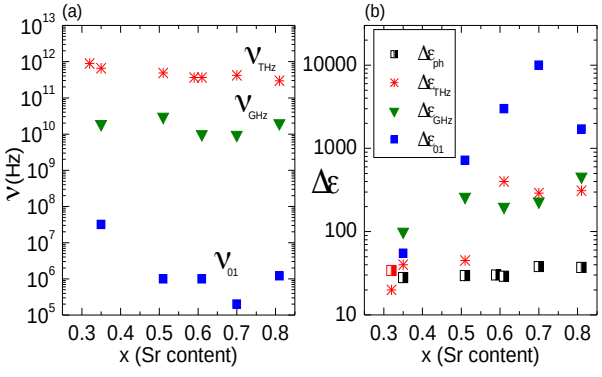

Figure 13: Composition dependences of the frequencies and the dielectric contribution of the main high-frequency excitations in SBN

(a) Frequencies and (b) dielectric contribution of three main excitations found below 3 THz in SBN at room temperature, together with the total contributions from phonons.

IV.2 Comparison of non-phononic excitations at room temperature in SBN

As the contribution from phonons is almost constant for all TTBs, we can compare the individual excitations found at frequencies below several THz. Their frequencies at room temperature are displayed in Fig. 13a. The CM, labelled ν_{THz}, has very similar frequency for all the compositions, although there is a monotonic decrease towards higher amounts of Sr. This could mean that the hopping frequency of the corresponding cation is lower and that the associated shift from its centred crystallographic position is probably larger. The excitation at GHz range shows very similar frequencies for all the family, although with the resolution of our experiments the accuracy is not enough to set a more precise frequency. The main relaxation, ν_{01}, shows also a decrease in frequency with the increase of Sr content. This can be understood as a link to the size of the polar entities responsible for it, which is much smaller for high Sr content crystals, showing utmost relaxor behaviour.

Fig. 13b shows the dielectric contribution of the same three excitations, and also the overall contribution from phonons, which is practically constant. For crystals with higher Sr-content crystals the dielectric contributions from the CM and the excitation at GHz are higher. If ν_{GHz} is related to oscillation of domain walls, we could deduce that the density of the domain walls is higher for the extreme relaxor samples (more Sr). Nevertheless, the origin of this excitation is still unclear and it could be also due to the presence of several polarization subsystems associated with the different shifts of the two Nb atoms in the crystal lattice [15,31]. The most important contribution to the permittivity arises from the relaxation ν_{01}, and it has no monotonic behaviour with Sr-content increase. It shows a maximum for the composition x=0.70 and then decrease. This relaxation slows down in all the studied composition, and is mostly responsible for the dielectric anomaly. It shows Vogel-Fulcher-Tammann (or simply Vogel-Fulcher)

behaviour for the intermediate compositions and Arrhenius behaviour for the extreme compositions *x*=0.35 (ferroelectric) and *x*=0.81 (relaxor). This relaxation has been associated with the diffuse scattering and specifically with flat discs with a correlation length of about 10 nm [34]. More diffuse scattering has been measured in SBN-35 and SBN-81 [35], and recently in SBN-60 [36]. The corresponding correlations lengths vary, being smaller for high Sr content compositions where the disorder is stronger.

The last investigations in SBN demonstrated that the existence of different crystallographic sites for the Nb atoms play a crucial role in the development of the ferroelectricity and the whole arrangement of the crystalline network[15]. Nb(1), placed inside the linking octahedra (dark blue octahedra in Fig. 1), has the tendency of being displaced mainly along the polar axis, which builts a fixed polarization network even at high temperatures, but scattered and unable to create a macroscopic spontaneous polarization. On the contrary Nb(2), located inside the octahedra of the perovskite sub-units of the TTB structure (light coloured octahedra in Fig. 1), tends to be shifted in the *ab* plane at high temperatures and does not contribute to the polarization. Only when the amount of Sr is small and the temperature is low enough, these Nb atoms start to shift along the polar axis and contribute also to the macroscopic polarization. Therefore SBN has two polarization subsystems that behave differently depending on the substitution ratio in the channels. The Nb shifts are probably mediated by the tilts of the NbO_6 octahedra network, which also depend on the cationic substitution ratio, although the precise mechanism is still under debate. When the amount of Sr is higher, the presence of more Sr atoms in the pentagonal channels affects the oxygen tilts pattern within the crystallographic structure. This, indirectly, disturb the correlated Nb shifts along the polar axis and seems to strengthen the relaxor behaviour.

The shift of Nb and also of Sr atoms in the *ab* plane creates the CM which plays an important role in the ferroelectric phase transition of SBN. This mode is also present in CBN, therefore the ferroelectric mechanism in this solid solution should be very similar. The presence of temperature dependent relaxations at lower frequencies with different temperature dependence (slowing down) is another polarization mechanism which contributes to the phase transition. This was found in SBN, but in CBN should be quite similar. Therefore the multiple polarization mechanisms with different correlation lengths and characteristic frequencies are the key to understand the ferroelectric phase transition in TTBs. The absence of a classic optical soft mode (presumably as result of the complicated arrangement of the oxygen octahedra network), is combined with the presence of a soft CM and the slowing down of a relaxation at GHz-MHz ranges. This, together with the results of the *ab-initio* calculations regarding the Nb shifts, speaks in favour of a mixed displacive–order-disorder scenario for the ferroelectric phase transition. However, it seems that the slowing down of a relaxation near the MHz range is the principal mechanism as it carries the main contribution to the dielectric anomaly in the studied TTBs.

V. Conclusions

The behaviour of phonons and relaxations has been investigated in two families of unfilled TTBs, namely SBN and CBN. The change of their parameters has been reported. Phonons change accordingly to the lowering of the symmetry, and give hints about the occupation in the channels, mainly the external phonons below 200 cm^{-1}. Our vibrational spectroscopic results show that, even though the occupation was supposed to be fixed for CBN (Ca in squared channels and Ba in pentagonal ones), there can be a small transfer of Ca into the pentagonal channels.

The phase transition in unfilled TTBs is not driven by phonons, but by excitations of lower frequency. Namely a central mode that softens and a relaxation in the GHz that slows down to the MHz-kHz range.

In SBN, the dielectric response is caused by several mechanisms with different frequencies, ranging from kHz to THz. There is no classical soft optical phonon, but a soft central mode, a relaxation at GHz frequencies related to domain walls oscillations or to smaller polar entities, and finally a relaxation that slows down related to nanosized polar fluctuations at high temperatures and then to the polar response of the ferroelectric domains of various sizes in the ferroelectric phase.

Acknowledgements:

This work was supported by the Czech Science Foundation (project no. 16-09142S).

Complementary informations on authors:

buixader@fzu.cz
ResearcherID: A-8109-2013, ORCID: https://orcid.org/0000-0001-8540-1441
jan.dec@us.edu.pl
ResearcherID: A-1021-2009, ORCID: https://orcid.org/0000-0003-4137-7018

Cite this paper: E. Buixaderas and J. Dec, OAJ materials and Devices, vol 5(1) – chap No8 in "Perovskites and other Framework Structure Crystalline Materials", p 281 (Coll. Acad. 2021) DOI:10.23647/ca.md20202108

REFERENCES

1. B. Jaffe, W.R. Cook, and H. Jaffe, Piezoelectric Ceramics (Academic Press, New York, 1971) p. 135.
2. D. P. Cann, C. A. Randall and T. R. Shrout, Investigation of the dielectric properties of bismuth pyrochlores, Sol. St. Comm. 100, 529 (1996).
3. R. E. Schaak and T.E. Mallouk, Perovskites bz design, Chem. Mat. 14, 1455 (2002).
4. A. Moure, Review and Perspectives of Aurivillius Structures as a Lead-Free Piezoelectric System, Appl. Sci. 8, 62 (2018).
5. A. Rotaru, A. J. Miller et al, Towards novel multiferroic and magneto-electric materials: dipole stability in tetragonal tungsten bronzes, Phil. Trans. Roy. Soc. A 372, 20120451 (2014).
6. X. Zhu, M. Fu, M. C. Stennett, P. M. Vilarinho, I. Levin, C. A. Randall, J.Gardner, F. D. Morrison, and I. M. Reaney, A Crystal-Chemical Framework for Relaxor versus Normal Ferroelectric Behavior in Tetragonal Tungsten Bronzes, Chem Mat 27, 3250 (2015).
7. T. Lukasiewicz, M.A. Swirkowicz, J. Dec, W. Hofman, W. Szyrski, Strontium–barium niobate single crystals, growth and ferroelectric properties, J. Crystal Growth 310, 1464 (2008).
8. M.D. Ewbanks, R.R. Neurgaonkar and W.K. Cory, Photorefractive properties of strontium□ barium niobate, J. Appl. Phys. 62, 374 (1987).
9. A. M. Glass, Investigation of the Electrical Properties of Sr 1−x Ba x Nb 2 O 6 with Special Reference to Pyroelectric Detection, J. Appl. Phys. 40, 4699 (1969).
10. H. Liu, J. Zhong, Ch. Lee, S.-W. Lee, and L. Lin, A comprehensive review on piezoelectric energy harvesting technology: Materials, mechanisms, and applications featured, App. Phys. Rev. 5, 041306 (2018).
11. H. Bai, J. Li, Y. Wu, Y. Hong, K. Shi, Z. Zho, Exploring determinants of lattice structure and high energy storage properties of Fe-doped SBN ceramics, Ceram Int. 45, 11109 (2019).
12. L.B. Kong, S. Li, T.S. Zhang, J.W. Zhai, F.Y.C. Boey, J. Mad, Electrically tunable dielectric materials and strategies to improve their performances, Progress in Materials Science 55, 840 (2010).
13. E. Buixaderas, M. Kempa, V. Bovtun et al, Multiple polarization mechanisms across the ferroelectric phase transition of the tetragonal tungsten bronze SBN-35, Phys Rev. Mat 2, 124402 (2018).
14. E. Buixaderas, C. Kadlec, M. Kempa, V. Bovtun, M. Savinov, P. Bednyakov, J. Hlinka and J. Dec, Fast polarization mechanism in the uniaxial tungsten-bronze relaxor SBN-81, Sci. Rep. 7, 18034 (2017).
15. M. Pasciak, P. Ondrejkovic, J. Kulda et al., A Phys Rev. B 99, 104102 (2019).
16. W. Hayes and R. Loudon, Scattering Of Light By Crystals, (Wiley And Sons New York, 1978)
17. T. C. Damen, S.P.S. Porto, B. Tell, Raman Effect in Zinc Oxide, Phys Rev. 142, 570 (1967).
18. G. Burns, J.D. Axe and D.F. O'Kane, Raman measurements of NaBa 2 Nb 5 O 15 and related ferroelectrics, Solid State Comm. 7, pp. 933-936, (1969).
19. A. Boudou and J. Sapriel, Phys. Rev. B 21, 61 (1980).
20. A. Speghini, M. Bettinelli, U. Caldiño, M. O. Ramírez, D. Jaque, L. E. Bausá and J. García Solé, Phase transition in Sr x Ba 1−x Nb 2 O 6 ferroelectric crystals probed by Raman spectroscopy, J. Phys. D: Appl. Phys. 39, 4930 (2006).
21. C. David, A. Tunyagi, K. Betzler, and M. Wöhlecke, Compositional dependence of optical and vibrational properties of strontium barium niobate Sr x Ba 1-x Nb 2 O 6 , Phys. stat. sol. (b) 244, 2127 (2007).
22. E. Buixaderas, I. Gregora, J. Hlinka, J. Dec and T. Lukasiewicz, Raman and IR phonons in Sr 0.35 Ba 0.69 Nb 2 O 6.04 single crystals, Phase Transit. 86, 217 (2013).
23. J. Ruiz-Fuertes, L. Bayarjargal, B. Winkler, M. Burianek, and M. Muhlberg, Polar nanoregions of Ca 0.28 Ba 0.72 Nb 2 O 6 probed by second harmonic generation and Raman spectroscopy at high pressure, App. Phys. Lett. 104, 262902 (2014).

24. H. R. Xia et al., Raman and infrared reflectivity spectra of potassium lithium niobate single crystals, Phys. Rev. B 55, 14892 (1997).
25. J. Alanis. M.C. Rodríguez□Aranda. Á.G. Rodríguez et al. Temperature dependence of the Raman dispersion of Sr 2 Nb 2 O 7 , J. Raman Spectrosc. 50, 102 (2018).
26. J. Dec, W. Kleemann, V.V. Shvartsman, D.C. Lupascu, T. Lukasiewicz, From mesoscopic to global polar order in the uniaxial relaxor ferroelectric Sr 0.8 Ba 0.2 Nb 2 O 6 , Appl. Phys. Lett. 100, 052903 (2012).
27. M. Eßer, M. Burianek, P. Held et al., Optical characterization and crystal structure of the novel bronze type Ca x Ba 1-x Nb 2 O 6 , Cryst. Res. Technol. 38, 457 (2003).
28. J. Hlinka, T. Ostapchuk, E. Buixaderas, C. Kadlec, P. Kuzel, I. Gregora, J. Kroupa, M. Savinov, A. Klic, J. Drahokoupil, I. Etxebarria, J. Dec, Multiple Soft-Mode Vibrations of Lead Zirconate, Phys. Rev. Lett. 112, 197601 (2014).
29. F. Gervais, Infrared and Millimeter waves, vol. 8, Chapter 7, edited by K. J. Button, (Ac. Press, New York, 1983), p. 279.
30. E. Buixaderas, M. Savinov, M. Kempa et al., Infrared and dielectric spectroscopy of the relaxor ferroelectric Sr 0.61 Ba 0.39 Nb 2 O 6 , J. Phys.: Condens. Matter 17, 653 (2005).
31. E. Buixaderas, M. Kempa, Š. Svirskas, C. Kadlec, V. Bovtun, M. Savinov, M. Paściak and J. Dec, Dynamics of mesoscopic polarization in uniaxial tetragonal tungsten-bronze (Sr x Ba 1-x)Nb 2 O 6 , Subm to Phys Rev. B (2019).
32. O. V. Malyshkina, V. S. Lisitsin, J. Dec and T. Lukasiewicz, Pyroelectric and Dielectric Properties of Calcium Barium Niobate Single Crystals, Phys. Solid State 56, 1824, (2014).
33. J. Dec, W. Kleemann, V.V. Shvartsman, D.C. Lupascu, T. Lukasiewicz, From mesoscopic to global polar order in the uniaxial relaxor ferroelectric Sr 0.8 Ba 0.2 Nb 2 O 6 , Appl. Phys. Lett. 100, 052903 (2012).
34. P. Ondrejkovič, M. Kempa, J. Kulda, B. Frick, M. Appel, J. Combet, J. Dec, T. Lukasiewicz, and J. Hlinka, Dynamics of Nanoscale Polarization Fluctuations in a Uniaxial Relaxor, Phys. Rev. Lett. 113, 167601 (2014).
35. M. Paściak, M. Kopecky, J. Kub, J. Fabry, J. Dec, P. Ondrejkovic, J. Hlinka and E. Buixaderas, X-ray diffuse scattering observations for Sr x Ba 1-x Nb 2 O 6 single crystals with x=0.35 and 0.81, Phase Transit. 91, 969 (2018).
36. P. Yu. Vanina, S. B. Vakhrushev, A.A. Naberezhnov and A. A. Bosak, Multiscale local ordering in the prototypical uniaxial relaxor Sr0.6 Ba0.4 Nb2O6 single crystal at room temperature, J. Phys.: Condens. Matter 31, 175401 (2019).
37. M. Eremenko, V. Krayzman, A. Bosak, et al. Local atomic order and hierarchical polar nanoregions in a classical relaxor ferroelectric, Nat. Comm. 10, 2728 (2019).
38. V.V. Shvartsman, D. Gobeljic, J. Dec and D.C. Lupascu, A Piezoresponse Force Microscopy Study of Ca x Ba 1-x Nb 2 O 6 Single Crystals, Materials 10, 1032 (2017).
39. E. Buixaderas, P. Bérešová, P. Ondrejkovič et al., Acoustic phonons in unfilled tetragonal tungsten-bronze crystals, Phase Transit. 91, 976 (2018).
40. V. V. Shvartsman, W. Kleemann, T. Łukasiewicz and J. Dec, Nanopolar structure in Sr x Ba 1−x Nb 2 O 6 single crystals tuned by Sr⁄Ba ratio and investigated by piezoelectric force microscopy, Phys. Rev. B 77, 054105 (2008).
41. K. Nakamoto, Infrared and Raman Spectra of inorganic and coordination compounds, Wiley and sons, sixth edition (2009).
42. S.D. Ross, The vibrational spectra of lithium niobate, barium sodium niobate and barium sodium tantalite, J. Phys C 3, 1785 (1970).
43. E. Buixaderas, S. Kamba and J. Petzelt, Polar phonons and far-infrared amplitudon in Sr 2 Nb 2 O 7 , J. Phys. Condens. Matt. 13, 2823 (2001).